Computational Screen of M2P Metal Phosphides for Catalytic Ethane Dehydrogenation

Journal:	*Catalysis Science & Technology*
Manuscript ID	CY-ART-03-2022-000602.R1
Article Type:	Paper
Date Submitted by the Author:	14-Jul-2022
Complete List of Authors:	Ko, Jeonghyun; University of Notre Dame, Chemical and Biomolecular Engineering Schneider, William; University of Notre Dame, Chemical and Biomolecular Engineering

SCHOLARONE™
Manuscripts

Computational Screen of M$_2$P Metal Phosphides for Catalytic Ethane Dehydrogenation

Jeonghyun Ko[†] and William F. Schneider[*,†,‡]

†*Department of Chemical and Biomolecular Engineering, University of Notre Dame, Notre Dame, IN 46556, United States*

‡*Department of Chemistry and Biochemistry, University of Notre Dame, Notre Dame, IN 46556, United States*

E-mail: wschneider@nd.edu

Abstract

Metal phosphides are promising catalysts for hydrocarbon transformations, but computational screening is complicated by their diverse structures and compositions. To disentangle structural from compositional contributions, here we explore the metal-rich M_2P (M = Fe, Co, Ni, Cu, Mo, Ru, Rh, Pd, Ag, Pt) series in hexagonal and orthorhombic structures that are common to a subset of these materials, using supercell density functional theory (DFT). To understand the contribution of metal choice to utility for catalytic ethane dehydrogenation (EDH), we compute and compare the adsorption of key EDH intermediates across low-index surface terminations. These materials expose both metal and phosphide sites. Calculations show that binding energies at metal sites correlate with the bulk metals, with P incorporation either enhancing or suppressing binding. Phosphide sites compete with metal sites for adsorbates and tend to suppress overactivation by destabilizing highly dehydrogenated species. engaging in C−H bond breaking. Results are generally insensitive to bulk structure and surface facet. Results suggest metal-rich Pd phosphides to have favorable adsorption characteristics for catalytic dehydrogenation, consistent with recent observations.

Keywords

Density functional theory, metal phosphide, dehydrogenation, ethane

1   Introduction

The discovery of abundant shale resources in the United States has resulted in gas liquids (NGLs) production to exceed their domestic consumption.[1–4] Ethane is the most prevalent component of NGLs, and dehydrogenation to ethylene is the first step in converting into a petrochemical feedstock.[3] Steam cracking of ethane is energy- and capital-intensive,[5,6] motivating the development of alternative and scalable dehydrogenation strategies.

Catalytic dehydrogenation of ethane $(C_2H_6 \longrightarrow C_2H_4 + H_2)$ is an alternative option to steam cracking for ethylene production. Ethane dehydrogenation (EDH) could operate with smaller and local processing plants than steam cracking. However, temperatures greater than 750°C are required to achieve $\geq$ 50 % conversion at atmospheric pressure. Catalyst selectivity and resistance to coke are both challenging at these harsh conditions. EDH catalysis is not practiced commercially today.

Smaller active metal ensembles are known to be effective in mitigating side reactions and coke formation during catalytic EDH.[7–11] Alloying a second metal (Sn,[7–9] Zn,[10] and In[11]) into Pt or Pd is observed to improve selectivity and catalyst stability. Similar to metal alloys, metal phosphides have been shown to offer potential as selective and robust EDH catalysts.[12–16] Recently, density functional theory (DFT) calculations, and spectroscopic and reaction measurements studies have shown that phosphorus addition into Ni[17] and Co[18] improves EDH selectivity and durability. A density functional theory (DFT) comparison of EDH performance on Ni(111) and $Ni_2P(001)$[17] showed that P atoms selectively participate in adsorbate binding and C−H bond breaking, increasing activation barriers for steps leading to deep dehydrogenation and promoting ethylene desorption over ethylene overactivation. In addition, P incorporation weakens binding of small hydrocarbons, imparting coke resistance to the surface. These two features are predicted to contribute to the remarkable product selectivity and intrinsic EDH activity of Ni_2P.

While recent work has focused on Ni- and Co-based phosphides as alkane dehydrogenation

catalysts,[17–22] other metal phosphides exhibit promising catalytic performance for other catalytic reactions.[12–16] Thus, an overall picture of EDH performance across metal phosphides is yet to be established. Because performance is closely linked to binding energies (either directly through adsorption/desorption steps or indirectly through Brønsted-Evans-Polanyi relationships), understanding trends in adsorption on metal phosphides is an important first step towards metal phosphide catalyst design for selective EDH. However, those trends may be sensitive to phosphide composition, bulk crystal structure, and even exposed facet.[23] The structural and compositional diversity of metal phosphides are substantial obstacles to interrogating metal phosphide chemistry in a consistent way.

There have been several attempts to examine general adsorption trends and/or catalytic behavior across metal phosphide surfaces using DFT.[24–28] One common approach is to screen across metal phosphides of different stoichiometry and to select low energy or common facets.[24,25] The Bravais-Friedel-Donnay-Harker (BFDH) algorithm, which is based on morphology of crystal structures, is useful for identifying low energy surface facets.[29,30] For example, Kibsgaard et al.[24] used BFDH to infer morphologically important facets (predicted to be common) of CoP, Co_2P, FeP, Fe_2P, Ni_2P and MoP as a basis for further analysis of hydrogen adsorption free energies (ΔG_H) of relevance to the hydrogen evolution reaction (HER). Another approach is to to dope the screening element of interest into a fixed phosphide structure and observe the effect on adsorption energy.[25–28] As a representative case, Partanen et al.[27,28] modeled Mg-, Mo-, Fe-, Co-, V- and Cu-doped Ni_3P_2-terminated $Ni_2P(001)$ to look at variations in ΔG_H with different dopants for HER. They predicted that thermodynamic stability and ΔG_H vary substantially with the number and identity of dopants. This approach exploits consistent geometric features to extract composition-specific information. Extending either approach to EDH is challenged by the diversity of potential phosphide structures and facets and the greater number and complexity of EDH-relevant intermediates than HER.

Research to date suggests that metal-rich phosphides hold the most promise as EDH

catalysts.[17–22] In this work, we use DFT models to explore the effect of geometric and chemical features on the adsorption energies of small hydrocarbons over the M_2P metal-rich phosphides. We construct geometrically consistent representations of M_2P structure, M = Fe, Co, Ni, Cu, Mo, Ru, Rh, Pd, Ag and Pt including both hexagonal (Ni_2P, Fe_2P) and orthorhombic (Co_2P, Ru_2P) structures that are common to a subset of these materials. We construct a consistent series of close-packed planes, and explore adsorption of EDH fragments across surfaces. We compare across bulk and surface representations and across metal- and phosphorus-centered adsorption sites to figure out P participation in adsorbate-binding. We show that adsorption energies vary with composition of metal phosphides, adsorption sites, in particular metal vs P sites. Lastly, we consider implications for EDH applications.

2   Computational Details

Density functional theory (DFT) calculations were performed with the Vienna Ab Initio Simulation Package (VASP).[31–33] Exchange-correlation energies were treated within the generalized gradient approximation (GGA)[34] using the Perdew-Burke-Ernzerhof (PBE) functional. Bulk lattice parameters were computed at a plane wave cutoff of 520 eV and slab calculations with a wave cutoff of 400 eV. Ni, Fe, Co, Fe_2P and Co_2P were performed spin-polarized; in test calculations, we found Ni_2P to have a negligible magnetic moment. GGA-computed lattice parameters are summarized in Table S1. Bulk hexagonal M_2P (space group $P\bar{6}2m$) consists of alternating M_3P_2 and M_3P_1 planes stacked along the [001] direction. Bulk orthorhombic M_2P (space group Pnma) has the same layer of M_2P stacked along the [001] direction. We chose the close-packed surface of the parent metals; Ni, Cu, Rh, Pd, Ag, Pt for fcc(111), Mo, Co and Ru for hcp(001), and bcc(110) for Fe. They were modeled with five-layer slabs. On the other hand, hexagonal M_2P(001)-A,B and orthorhombic (010) surfaces were modeled with six-layer slabs. For all metal and metal phosphide surfaces, we introduced a vacuum spacing of 15 Å. The bottom three layers were fixed at their bulk posi-

tions, and the remaining layers and adsorbates fully relaxed. (3×3) and (1×1) surface unit cells were employed for parent metal and M_2P surfaces. Monkhorst-Pack grids[35] of $3 \times 3 \times 1$, $7 \times 7 \times 1$ and $7 \times 8 \times 1$ **k**-points were selected for metal surfaces, hexagonal $M_2P(001)$ and orthorhombic $M_2P(010)$.

Geometries were relaxed to minima using the conjugate gradient algorithm until forces on unconstrained atoms were less than 0.02 eV/Å. The adsorption energy (E_{ads}) is defined as

$$E_{ads} = E_{total} - E_{slab} - E_{adsorbate} \tag{1}$$

Here, E_{total} is the total energy of the system with adsorbed species, E_{slab} is the total energy of the surface, and $E_{adsorbate}$ is the gas-phase energy of the adsorbate. The climbing image-nudged elastic band (CI-NEB) method was employed to determine the minimum energy paths and calculate the activation energies for surface reactions.[36] The vibrational spectra were obtained by calculating the Hessian matrix with finite differences of 0.015 Å. Each transition state was verified to have a single imaginary frequency along the reaction coordinate. All atomic positions after geometry optimizations with corresponding energy profiles are provided in SI. To identify the amount of charge transfer between metal and P atoms, Bader charge analysis was employed.[37–39]

3 Results and Discussion

3.1 Bulk models

We created isostructural hexagonal and orthorhombic M_2P series (M = Fe, Co, Ni, Cu, Mo, Ru, Rh, Pd, Ag, and Pt), shown in Figure 1. Hexagonal M_2P is the equilibrium crystal structure of Ni_2P and Fe_2P, and orthorhombic M_2P is that of Co_2P and Ru_2P.[40,41] To minimize effects arising from gross structural differences between the hexagonal and

orthorhombic crystal structures, we focused on the close-packed flat surface terminations, including hexagonal (001) and orthorhombic (010) facets (Figure 1). We took two different terminations from hexagonal (001) because alternating planes of Ni_3P_2("A") and Ni_3P_1("B") are stacked along the [001] direction while orthorhombic (010) is the only facet along the [010] direction.
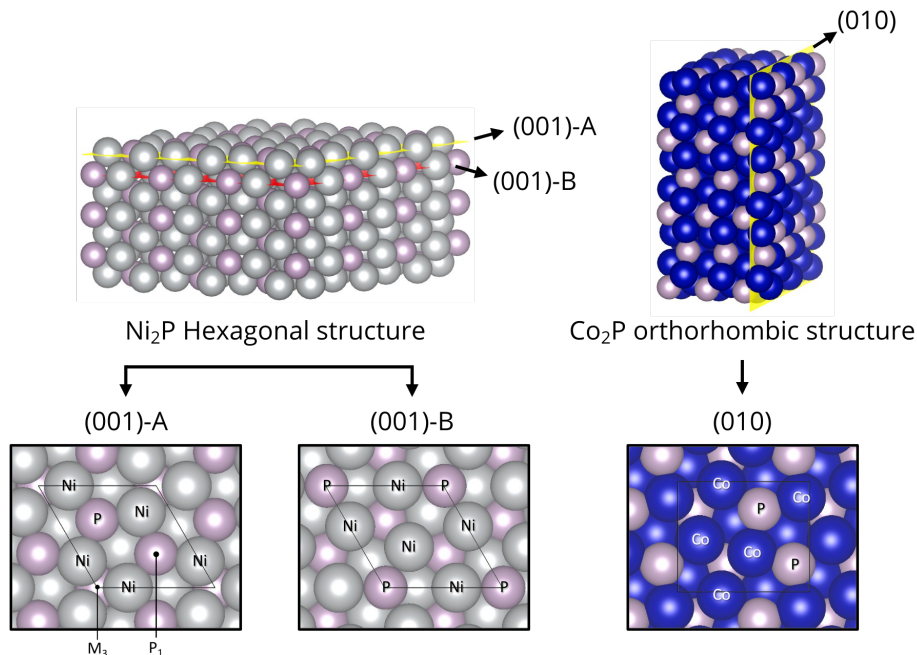
Figure 1: Bulk hexagonal Ni_2P, and orthorhombic Co_2P structures and their facets. Ni, Co and P atoms are shown in gray, blue and lavender, and adsorption sites labeled on hexagonal (001)-A surface.

Figure 2 reports computed formation energies relative to bulk metal and phosphorus $(E_f = E_{M_2P} - 2E_{M_{bulk}} - E_{P_{bulk}})$ of the orthorhombic and hexagonal M_2P structures. Here E_{M_2P}, $E_{M_{bulk}}$ and $E_{P_{bulk}}$ are the total energy of bulk M_2P, parent metal and red phosphorous, respectively. Formation energies are negative except for Cu_2P and Ag_2P. Formation energies of hexagonal (red circle) and orthorhombic (blue circle) are almost identical. We use hull distance to evaluate the stability of a compounds with respect to another phase or combination of phases.[42] The green data in Figure 2 correspond to the formation energies of the M_2P phase on the convex hull if one exists and is neither hexagonal nor orthorhombic. If a stable M_2P phase is unknown, we computed formation energies of ground state structures

of bounding compositions and report in Figure 2 the energy of the tie line at M_2P as unfilled green circles.[42,43] For example, a stable Mo_2P phase is unknown. We computed the formation energies of the known MoP (Mo/P=1) and Mo_3P (Mo/P=3) phases, constructed the tie line between the two, and report in Figure 2 the energy of the tie line at Mo/P=2. Thus, hexagonal and orthorhombic Pd_2P, Mo_2P, Rh_2P, Ag_2P and Pt_2P are thermodynamically unstable to phase separation, Pd_2P least so, and Pt_2P most so.
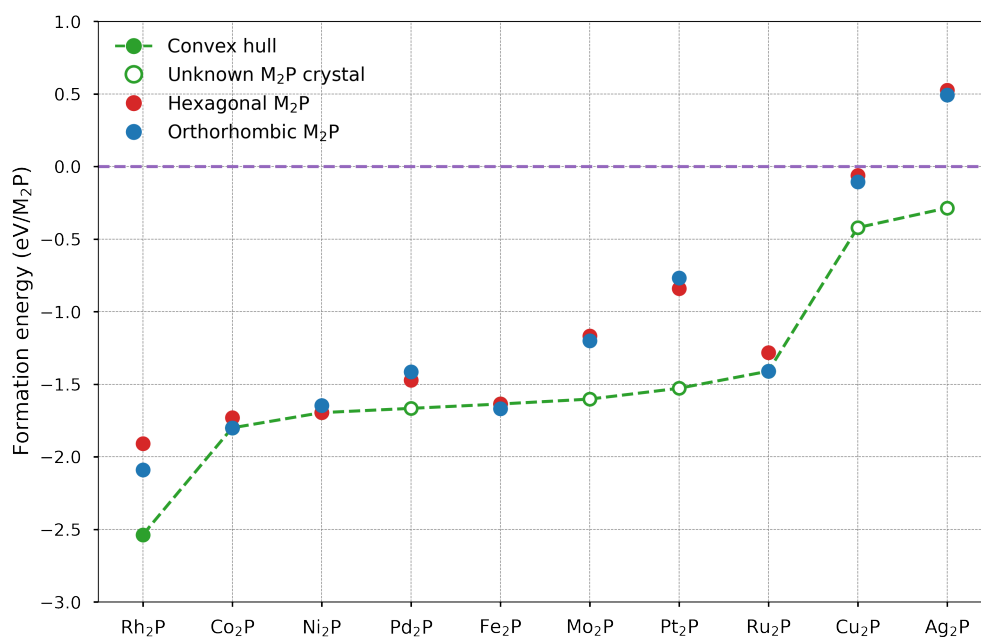
Figure 2: Formation energies (E_f) of hexagonal (red) and orthorhombic (blue) M_2P structures. E_f of most stable M_2P structure if one exists (solid green), or energy of tie line between structures of bounding compositions (open green).

We performed Bader charge analysis on both hexagonal and orthorhombic bulk structures to quantify the electronic state changes with respect to elements and coordinations. Hexagonal M_2P contains tetrahedral (T) and square pyramidal (SP) metal sites as well as two inequivalent tetrakaidecahedral (TKD) P sites, which we label TKD1 and TKD2, respectively. Orthorhombic M_2P also has T and SP metal sites, but a single P TKD. These sites are illustrated in Figure 3.
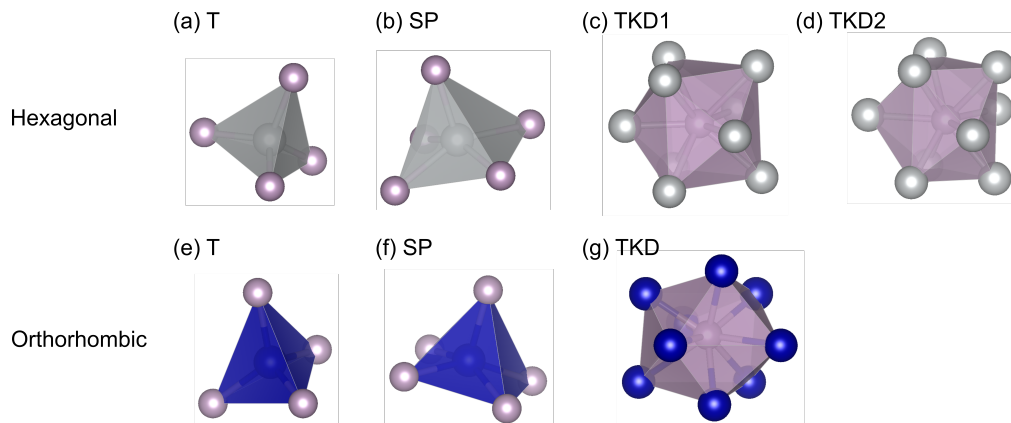
Figure 3: Atomic coordinations of metal and P atoms in hexagonal Ni_2P ((a)-(d)) and orthorhombic Co_2P ((e)-(g)) structures. T and SP are tetrahedral and square pyramidal sites for metal atoms, respectively. TKD is tetrakaidecahedral site for P atoms. Ni, Co and P atoms are shown in gray, blue and lavender, respectively.

Figure 4a and b report computed Bader charges on metal and phosphorus sites in the hexagonal and orthorhombic structures, respectively. Despite the consistent stoichiometry, charges vary widely with composition; phosphorus charges vary from near $+0.4e$ with the most electronegative metal (Pt) to $-1.0e$ on the most electropositive (Mo). Metal charges vary proportionally and in the opposite direction. Results are generally consistent with electronegativity differences and DFT computed-charge states of other common phosphides.[15,44] Thus, it would be inappropriate to think of the metals as having a single formal charge across the series. Trends are slightly sensitive to metal coordination numbers and essentially insensitive to bulk structure.

3.2   Metal and metal phosphide adsorption energies

We next cleaved and relaxed the bulk structures to generate the surfaces shown in Figure 1. All surfaces save the Pt_2P case retained the same equilibrium structure. In the Pt_2P case, sublayer P atoms migrate to the surface and isolate surface Pt atoms, destroying the Pt_3 ensemble (shown in Figure S1). This instability is consistent with the large distance of the hypothetical Pt_2P structures above the tie line (Figure 2). We thus excluded Pt_2P from adsorbate comparisons. Figure S2 reports atom-projected densities of states of the remaining

(a)

(b)
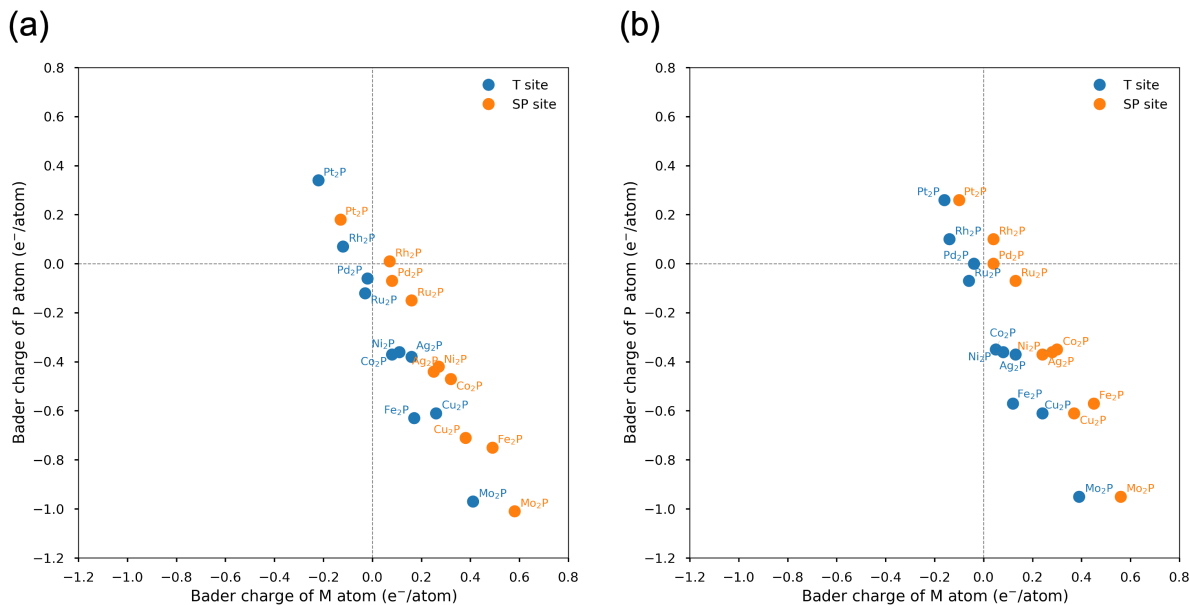
Figure 4: Bader charge of metal and P atoms in (a) hexagonal and (b) orthorhombic M_2P bulk structures. Metal T and SP sites were compared to phosphorous TKD sites, respectively.

surfaces. Phosphorus p states are generally broad and low in energy. Interactions with P broadens and splits the metal d states, which dominate the states near the Fermi level for all compounds save Pd_2P, Cu_2P and Ag_2P. As with charges, DOS are generally insensitive to structure. Figure S3 reports d band centers relative to the Fermi level for the $M_2P(001)$-A surface vs d band centers of the corresponding metal surfaces. Phosphorus incorporation results in a downward shift of d centers for almost all phosphides, especially pronounced for Cu_2P and Pd_2P. Shifts are generally insensitive to structure (Table S2).

Given that electronic structure appears to be insensitive to bulk structure and local site coordination, we first consider adsorption chemistry on the hexagonal $M_2P(001)$-A facet. We select H, CH_3, CH, and C as probes of saturated (sp^3), unsaturated (sp) and carbonaceous adsorbates and compute adsorption at the M_3 sites (shown in Figure 1). We also compute adsorption on the corresponding site on the parent metal to assess the influence of P incorporation on adsorption. Adsorbates were placed above the center of the three-fold (M_3) site and relaxed. All relaxed structures are provided in the SI. The addition of adsorbates results in a general contraction in the trimeric metal ensemble ($-0.28\,\text{Å} \leq \Delta d_{M-M} \leq -0.01\,\text{Å}$). In

some cases, adsorbates relaxed away from the M_3 sites to 2-fold or 4-fold sites (e.g., C on Fe(110)). These cases were excluded from the analysis as well.

Figure 5 reports parity plots of the binding energies on the phosphide surface vs the metal. Energies span similar ranges on the metal and phosphide and are roughly linearly correlated but do not exhibit a consistent shift as might be expected from the d band center comparisons. Significant positive and negative deviations are evident, large enough to alter binding energy orderings. Binding energies on $Ni_2P(001)$-A and $Pd_2P(001)$-A are always less negative than on the parent metals. $Pd_2P(001)$-A is the most extreme outlier. P addition into Pd increases binding energies from $0.47\,eV$ for CH_3 up to $1.97\,eV$ for C. In contrast, P addition results in negative deviations on $Co_2P(001)$-A and $Fe_2P(001)$-A. On the other metal phosphides, deviations are adsorbates-specific. These deviations in binding energies from the parity line do not correlate with M_3 ensemble size, lattice parameters, adsorbate-induced surface relaxation, or other geometric features. As shown in Figure S4, metal site adsorption energies roughly correlate with d band center shift, although again significant outliers are present.

Previous DFT calculations of EDH reaction paths on $Ni_2P(001)$ reveal that surface P atoms do participate in some C$-$H bond cleavage steps.[17] This selective participation is related to the preference of sp^2 and sp^3 C for P sites, which is computed to increase the activation energies of deep dehydrogenation steps over the bulk metal and thus to enhance ethylene selectivity. As shown in the the inset of Figure 6, CH_3 can bind both in the three-fold metal hollow and atop P; binding energies on these two sites are nearly the same.[17] We performed similar comparisons using CH_3 as a probe of metal vs P preference across the M_2P series. We relaxed CH_3 at M_3 and atop P sites (shown in the inset of Figure 6) and compared adsorption energies. Resultant optimized structures of P site binding are provided in SI. CH_3 binding energies at atop P sites are plotted against M_3 sites in Figure 6. Binding energies are roughly anti-correlated, with earlier and less noble d block metals generally exhibiting stronger binding at metal than P sites. The P site is preferred for the later metals
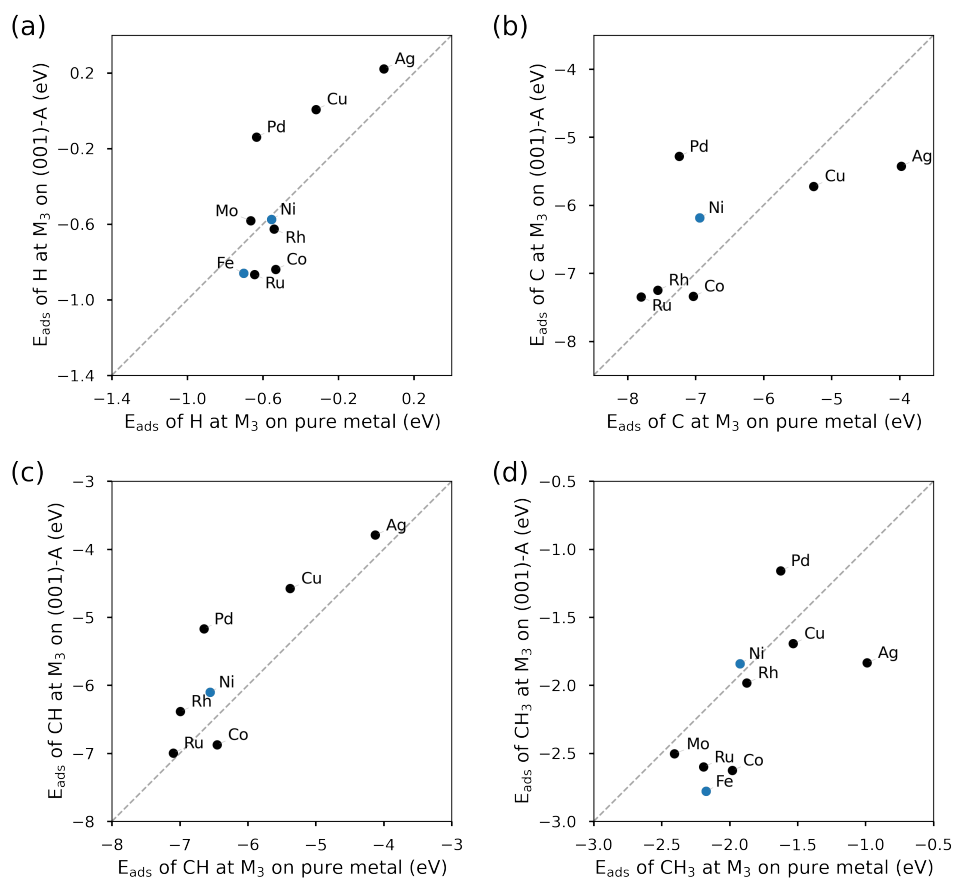
Figure 5: Adsorption energies of (a) H, (b) C, (c) CH and (d) CH_3 on hexagonal $M_2P(001)$-A plotted against adsorption energies on the corresponding metals. Blue markers highlight compounds that are stable in the hexagonal M_2P structure.

$Cu_2P(001)$-A, $Pd_2P(001)$-A and $Ag_2P(001)$-A, which are similarly the phosphides that have a large contribution of phosphorus p states at the Fermi level and low-lying metal d states (Figure S3). Phosphorus sites are thus expected, as with Ni_2P, to have a strong influence on C−H activation steps.
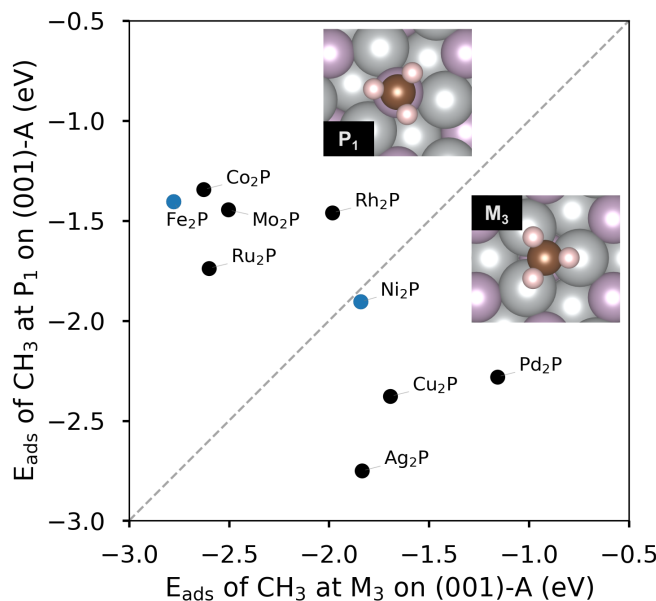
Figure 6: CH_3 adsorption energies at P_1 sites plotted against M_3 sites on on hexagonal $M_2P(001)$-A. Blue markers highlight compounds that are stable in the hexagonal M_2P structure.

We repeated H, C, CH, CH_3 relaxation calculations at the M_3-centered sites on hexagonal $M_2P(001)$-B and orthorhombic $M_2P(010)$ surfaces. In some cases, adsorbates (especially C atoms) move away from M_3 sites to atop or bridge sites or move subsurface. These cases were excluded from our energy comparisons to assure consistency. E_{ads} are summarized in Supplementary Tables S4-S6. Figure 7a reports H adsorption energies on the $M_2P(001)$-B and $M_2P(010)$ surfaces vs adsorption energies on $M_2P(001)$-A; panels b-d report similar comparisons for C, CH, CH_3, respectively. The results in panels b-d show that hydrocarbon binding energies at metal sites are generally insensitive both to bulk structure and surface termination. Largest deviations from parity are $0.83\,eV$, and are small relative to variations with metal. In contrast, and as highlighted in panel a, H binding energies evidence greater

13

sensitivity to structure. Deviations from parity increase from the earlier to the later metals. The most dramatic example is H binding on the $Ag_2P(001)$ A and B facets; these differences do not appear to have an origin in differences in structure (Figure S5 in SI). Missing points in Figure 7, including H on orthorhombic Ni_2P, Pd_2P and Cu_2P, correspond to cases in which adsorbates migrate from the M_3 to other sites or subsurface.

We also compared M_3 and P-site binding energies across the hexagonal $M_2P(001)$-B and orthorhombic $M_2P(010)$ surfaces (SI Table S7). Figure 8 plots adsorption energies at P sites against M_3 sites across all metals and structures. Spontaneous migration of CH_3 from M_3 to atop M or M−M bridge sites were observed especially on orthorhombic (010). Those cases were excluded in this analysis. General trends are consistent with Figure 6. Structure has a large effect for some metals, prominent among them Fe.

3.3 Implication for EDH catalyst

The results above highlight large scale trends in expected reactivity of metal-rich phosphides and the varying extent of participation of P in surface chemistry. Next we leverage those insights and results towards selection of EDH candidate materials.

Prior work suggests that the EDH ethylene selectivity and coking resistance imparted by converting Ni into Ni_2P can be traced to the weaker binding of small hydrocarbons on Ni_2P than Ni and the preference of sp^2 and sp^3 C centers for P sites.[17] We selected C and CH as binding energy probes because they are common fragments arising from C−C cleavage of C_2 species. Figure 9 compares the adsorption energies of C and CH on hexagonal $M_2P(001)$-A to those on Pt(111) and $Ni_2P(001)$-A, chosen as representative metallic (and quickly deactivating) and higher performing phosphide EDH catalysts. Data are taken from Figure 5. Fragment binding energies are greater on most of the other phosphides than on $Ni_2P(001)$-A and in many cases are even comparable to binding energies on Pt(111). The exceptions include the late metal phosphides $Cu_2P(001)$-A, $Pd_2P(001)$-A and $Ag_2P(001)$-A. Further, and as shown in Figure 6, CH_3 prefers phosphide over metal sites on these late
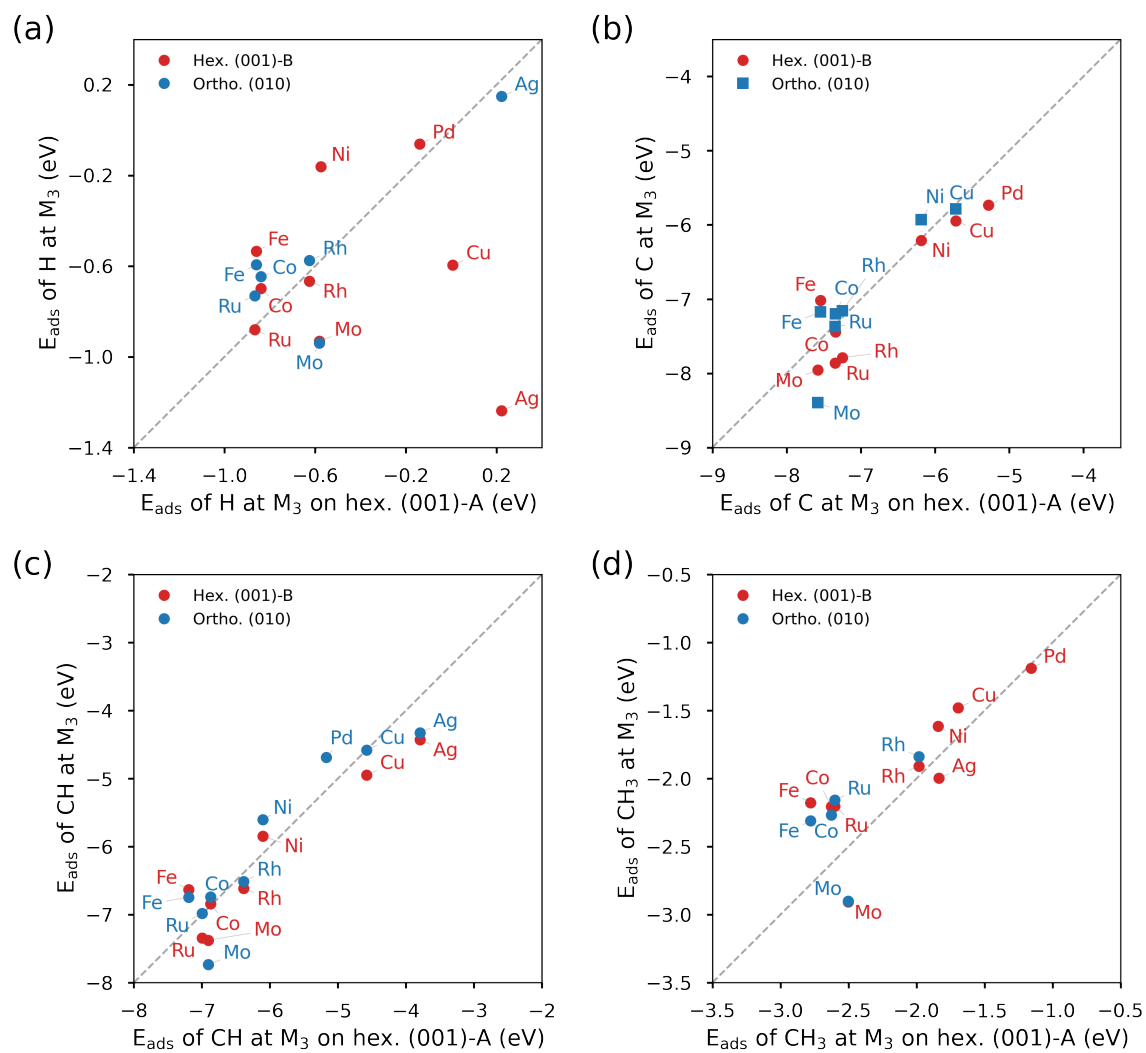
Figure 7: Parity plot comparison of adsorption energies at M-centered sites on hexagonal $M_2P(001)$-B and orthorhombic $M_2P(010)$ vs. those on hexagonal $M_2P(001)$-A.
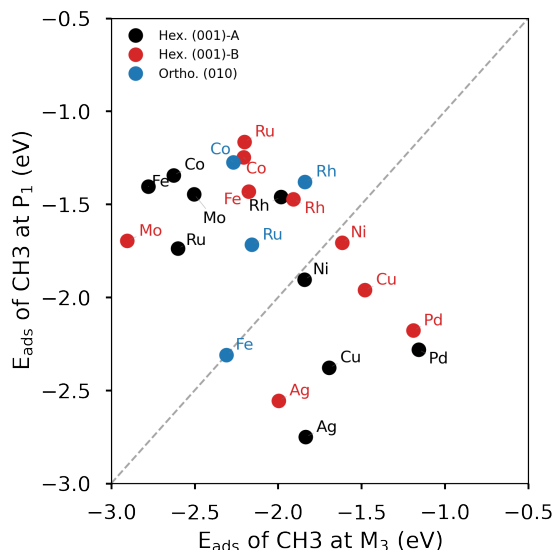
Figure 8: Comparison of adsorption site preference of CH_3 at M-centered sites on hexagonal $M_2P(001)$-A,B and orthorhombic $M_2P(010)$.

metal phosphides, as was found to be an important feature underlying the EDH activity on Ni_2P. Thus, the Cu_2P, Pd_2P, and Ag_2P (001) facets share many of the same favorable EDH features as does Ni_2P.

Metal-rich Cu−P and Ag−P phases are yet to be reported,[45,46] consistent with the large distance of the bulk M_2P compounds above the formation energy hulls (Figure 2). In contrast, several metal-rich Pd phosphides are known, including Pd_5P_2, Pd_3P and Pd_6P,[47–50] consistent with the short distance of Pd_2P above the hull. Thus, we chose Pd_2P for further investigation.

The difference between ethylene desorption ($C_2H_4{}^* \longrightarrow C_2H_4(g) + {}^*$) and ethylene dehydrogenation ($C_2H_4{}^* + {}^* \longrightarrow C_2H_3{}^* + H^*$) energies is a common descriptor for EDH selectivity. We chose $C_2H_4{}^*$ at atop Pd (the lowest energy) and Pd−P bridge (local minimum) sites as initial states. Then we sampled an H atom around the $C_2H_3{}^*$ at the lowest energy site (P_1) as well as local minima sites (Pd−Pd bridge, Pd−P bridge) to find co-adsorption configurations of $C_2H_3{}^*$ and H^* (final states). Those initial and final states were used as endpoints for reaction pathways for activation of H−$C_2H_3{}^*$; the three different ethylene dehydrogenation pathways obtained from this analysis are shown in Figure 10. C−H bond cleavage takes

place at the Pd_3 site in pathway 1 and across the Pd−P bridge in pathway 2. After C−H bond cleavage, C_2H_3 diffuses to a Pd−P bridge site and H remains at the Pd-Pd bridge site in pathway 1 while dissociated H and C_2H_3 rotate slightly to reach their favored adsorption configurations in pathway 2. Energy differences between the two transition states are about $0.38\,eV$. In pathway 3, C_2H_4 starts at a slightly energy Pd−P bridge site. Similar to pathway 2, the C−H bond cleaves across a Pd−P bridge and H migrates to a Pd−Pd bridge site. Ethylene activation energies across all these pathways greatly exceed the ethylene desorption energy.

We repeated the same calculations on hexagonal $Fe_2P(001)$-A and $Ni_2P(001)$-A as contrasts to $Pd_2P(001)$-A. Fe_2P strongly binds adsorbates and has a strong preference to bind those adsorbates at metal sites, opposite the adsorption characteristics of Pd_2P. On the other hand, the characteristics of Ni_2P place it in the middle between Fe_2P and Pd_2P. Ethylene dehydrogenation energy profiles and geometric structures computed on the (001)-A facets are summarized in Figures S6 and S7 of the SI. Due to the strong affinity of an Fe site for adsorbates, bond breaking takes place preferentially at Fe_2P metal sites (Figure S7a) with very small barriers; further; product ethylene is strongly surface-bound (Figure S6a). Ethylene dehydrogenation is more highly activated and ethylene desorption more accessible on $Ni_2P(001)$-A (Figure S7b), and both Ni or P sites potentially contribute to undesired C−H cleavage (Figure S6b). Those undesired pathways become even less favorable on Pd_2P, while ethylene desorption becomes even readier (Figure S6b, c). These calculations reinforce inferences from the C and CH binding energy trends, that the predicted EDH selectivity will follow $Pd_2P > Ni_2P >> Fe_2P$.

Thus, results suggest that the Pd phosphides as potential candidates for selective EDH. Literature observations support this prediction. Pd phosphides have recently been explored for the selective dehydrogenation of hydrocarbons.[48–50] Sampath and Flaherty[50] in particular used temperature programmed reaction (TPR) and reactive molecular beam scattering (RMBS) to compare C_6H_{10} dehydrogenation over Pd and metal-rich Pd_3P phosphide. Se-

lectivity to C_6H_6 is much greater over the Pd phosphide than Pd. Further, RMBS results suggest the phosphide to be more resistant to over dehydrogenation than is the metal.
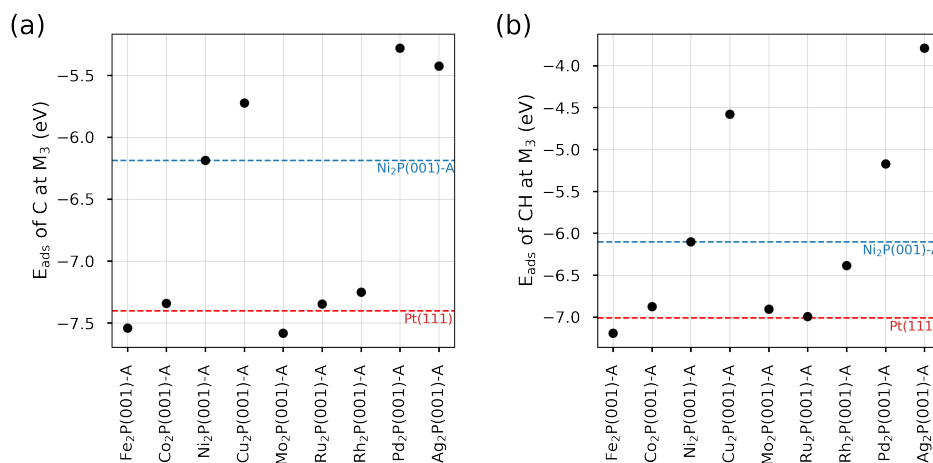
Figure 9: Comparison of adsorption energies of (a) C and (b) CH over hexagonal $M_2P(001)$-A to those over Pt(111) (red dashed line) and $Ni_2P(001)$-A (blue dashed line).
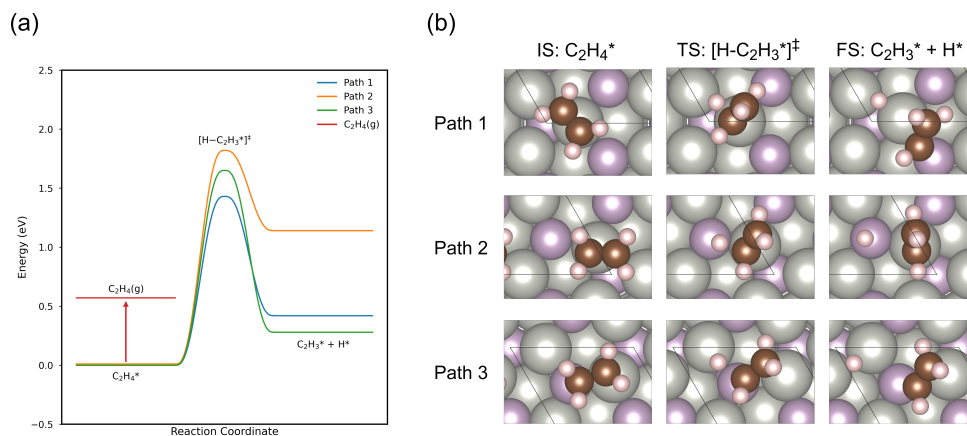
Figure 10: (a) Comparison of three possible ethylene dehydrogenation pathways vs ethylene desorption on hexagonal $Pd_2P(001)$-A. (a) Energy profiles of each pathway on $Pd_2P(001)$-A. (b) Geometric structures of initial state (IS), transition state (TS) and final state (FS) of three possible ethylene dehydrogenation pathways on $Pd_2P(001)$-A.

4   Conclusions

Computational screening is a powerful technique for identifying new solid catalysts with desirable activity and selectivity. Metal phosphides are promising candidates for catalytic

reactions involving C−H activation, but screening across metal phosphides is complicated by the large compositional and structural spaces as well as evidence that both metal and phosphorous sites participate in catalysis and contribute to observed selectivity. As a simple strategy to overcome some of these challenges, here we explore the surface chemistry of a series of isostructural metal-rich phosphides, some of which are stable compounds on the respective phase diagrams and some of which lie above known formation energy hulls. We compare a series of probe molecule bindings across a structurally consistent series of surface facets. Results are sensitive to metal but insensitive to structure, suggesting that the approach provides at least qualitative guidance in choice of phosphide for ethylene dehydrogenation. Analysis points to a metal-rich Pd phosphide as having desirable surface-chemical properties for selective EDH, a prediction at least qualitatively consistent with literature observation. While precise predictions clearly will be sensitive to precise structures and compositions, the approach offers an efficient first screen for phosphides and potentially other two-component systems (sulfides, nitrides, carbides) of interest for catalysis.

5　Acknowledgements

6　Conflicts of interest

There are no conflicts to declare.

7   Supporting information

DFT-computed lattice constants of hexagonal and orthorhombic M_2P, and pure metals; band structure analyses; summary of adsorption energies at M_3 and P_1 sites on hexagonal and orthorhombic M_2P and pure metal surfaces; vibrational frequencies of transition states for $H-C_2H_3$ on $Pd_2P(001)$-A; relaxed structures of hexagonal $Pt_2P(001)$-A,B and orthorhombic $Pt_2P(010)$. Zenodo repository available at `https://doi.org/10.5281/zenodo.6824056` contains the input files (INCAR, KPOINT) for VASP, and the full set of CONTCARs for all the structures discussed in the manuscript.

References

(1) Bruijnincx, P. C. A.; Weckhuysen, B. M. Shale Gas Revolution: An Opportunity for the Production of Biobased Chemicals? Angewandte Chemie International Edition **2013**, 52, 11980–11987.

(2) Stangland, E. E. Shale Gas Implications for C2-C3 Olefin Production: Incumbent and Future Technology. Annual Review of Chemical and Biomolecular Engineering **2018**, 9, 341–364.

(3) Sattler, J. J. H. B.; Ruiz-Martinez, J.; Santillan-Jimenez, E.; Weckhuysen, B. M. Catalytic Dehydrogenation of Light Alkanes on Metals and Metal Oxides. Chemical Reviews **2014**, 114, 10613–10653.

(4) National Academies of Sciences, E.; Studies, D.; Technology, B.; Alper, J. The Changing Landscape of Hydrocarbon Feedstocks for Chemical Production: Implications for Catalysis: Proceedings of a Workshop; National Academies Press, 2016.

(5) Wilczewski, W. U.S. Energy Information Administration - EIA - Independent Statistics and Analysis. 2015; `https://www.eia.gov/todayinenergy/detail.php?id=19771`.

(6) Ridha, T.; Li, Y.; Gençer, E.; Siirola, J.; Miller, J.; Ribeiro, F.; Agrawal, R. Valorization of Shale Gas Condensate to Liquid Hydrocarbons through Catalytic Dehydrogenation and Oligomerization. Processes **2018**, 6, 139.

(7) Hook, A.; Massa, J. D.; Celik, F. E. Effect of Tin Coverage on Selectivity for Ethane Dehydrogenation over Platinum–Tin Alloys. The Journal of Physical Chemistry C **2016**, 120, 27307–27318.

(8) Galvita, V.; Siddiqi, G.; Sun, P.; Bell, A. T. Ethane dehydrogenation on Pt/Mg(Al)O and PtSn/Mg(Al)O catalysts. Journal of Catalysis **2010**, 271, 209–219.

(9) Wu, J.; Peng, Z.; Bell, A. T. Effects of composition and metal particle size on ethane dehydrogenation over PtxSn100-x/Mg(Al)O (70≤x≤100). Journal of Catalysis **2014**, 311, 161–168.

(10) Cybulskis, V. J.; Bukowski, B. C.; Tseng, H.-T.; Gallagher, J. R.; Wu, Z.; Wegener, E.; Kropf, A. J.; Ravel, B.; Ribeiro, F. H.; Greeley, J.; Miller, J. T. Zinc Promotion of Platinum for Catalytic Light Alkane Dehydrogenation: Insights into Geometric and Electronic Effects. ACS Catalysis **2017**, 7, 4173–4181.

(11) Wegener, E. C.; Wu, Z.; Tseng, H.-T.; Gallagher, J. R.; Ren, Y.; Diaz, R. E.; Ribeiro, F. H.; Miller, J. T. Structure and reactivity of Pt–In intermetallic alloy nanoparticles: Highly selective catalysts for ethane dehydrogenation. Catalysis Today **2018**, 299, 146–153.

(12) Bonita, Y.; O'Connell, T. P.; Miller, H. E.; Hicks, J. C. Revealing the Hydrogenation Performance of RuMo Phosphide for Chemoselective Reduction of Functionalized Aromatic Hydrocarbons. Industrial & Engineering Chemistry Research **2019**, 58, 3650–3658.

(13) Pei, Y.; Cheng, Y.; Chen, J.; Smith, W.; Dong, P.; Ajayan, P. M.; Ye, M.; Shen, J.

Recent developments of transition metal phosphides as catalysts in the energy conversion field. Journal of Materials Chemistry A **2018**, 6, 23220–23243.

(14) Rensel, D. J.; Rouvimov, S.; Gin, M. E.; Hicks, J. C. Highly selective bimetallic FeMoP catalyst for C–O bond cleavage of aryl ethers. Journal of Catalysis **2013**, 305, 256–263.

(15) Rensel, D. J.; Kim, J.; Jain, V.; Bonita, Y.; Rai, N.; Hicks, J. C. Composition-directed FeXMo2-XP bimetallic catalysts for hydrodeoxygenation reactions. Catalysis Science & Technology **2017**, 7, 1857–1867.

(16) Cho, A.; Shin, J.; Takagaki, A.; Kikuchi, R.; Oyama, S. T. Ligand and Ensemble Effects in Bimetallic NiFe Phosphide Catalysts for the Hydrodeoxygenation of 2-Methyltetrahydrofuran. Topics in Catalysis **2012**, 55, 969–980.

(17) Ko, J.; Muhlenkamp, J. A.; Bonita, Y.; LiBretto, N. J.; Miller, J. T.; Hicks, J. C.; Schneider, W. F. Experimental and Computational Investigation of the Role of P in Moderating Ethane Dehydrogenation Performance over Ni-Based Catalysts. Industrial & Engineering Chemistry Research **2020**, 59, 12666–12676.

(18) Muhlenkamp, J. A.; LiBretto, N. J.; Miller, J. T.; Hicks, J. C. Ethane dehydrogenation performance and high temperature stability of silica supported cobalt phosphide nanoparticles. Catalysis Science & Technology **2022**, 12, 976–985.

(19) Xu, Y.; Sang, H.; Wang, K.; Wang, X. Catalytic dehydrogenation of isobutane in the presence of hydrogen over Cs-modified Ni 2 P supported on active carbon. Applied Surface Science **2014**, 316, 163–170.

(20) Xu, Y.; Wang, X.; Lv, R. Interaction between Cs and Ni2P/SiO2 for enhancing isobutane dehydrogenation in the presence of hydrogen. Reaction Kinetics, Mechanisms and Catalysis **2014**, 113, 393–406.

(21) Yao, Y.; Zuo, M.; Zhou, H.; Li, J.; Shao, H.; Jiang, T.; Liao, X.; Lu, S. One-Pot Preparation of Ni2P/γ-Al2O3 Catalyst for Dehydrogenation of Propane to Propylene. ChemistrySelect **2018**, _3_, 10532–10536.

(22) Zhu, Q.; Zhang, H.; Zhang, S.; Wang, G.; Zhu, X.; Li, C. Dehydrogenation of Isobutane over a Ni–P/SiO2 Catalyst: Effect of P Addition. Industrial & Engineering Chemistry Research **2019**, _58_, 7834–7843.

(23) Oyama, S. T.; Gott, T.; Zhao, H.; Lee, Y.-K. Transition metal phosphide hydroprocessing catalysts: A review. Catalysis Today **2009**, _143_, 94–107.

(24) Kibsgaard, J.; Tsai, C.; Chan, K.; Benck, J. D.; Nørskov, J. K.; Abild-Pedersen, F.; Jaramillo, T. F. Designing an improved transition metal phosphide catalyst for hydrogen evolution using experimental and theoretical trends. Energy & Environmental Science **2015**, _8_, 3022–3029.

(25) Fields, M.; Tsai, C.; Chen, L. D.; Abild-Pedersen, F.; Nørskov, J. K.; Chan, K. Scaling Relations for Adsorption Energies on Doped Molybdenum Phosphide Surfaces. ACS Catalysis **2017**, _7_, 2528–2534.

(26) Wexler, R. B.; Martirez, J. M. P.; Rappe, A. M. Chemical Pressure-Driven Enhancement of the Hydrogen Evolving Activity of Ni2P from Nonmetal Surface Doping Interpreted via Machine Learning. Journal of the American Chemical Society **2018**, _140_, 4678–4683.

(27) Partanen, L.; Hakala, M.; Laasonen, K. Hydrogen adsorption trends on various metal-doped Ni2P surfaces for optimal catalyst design. Physical Chemistry Chemical Physics **2019**, _21_, 184–191.

(28) Partanen, L.; Alberti, S.; Laasonen, K. Hydrogen adsorption trends on two metal-doped Ni2P surfaces for optimal catalyst design. Physical Chemistry Chemical Physics **2021**, _23_, 11538–11547.

(29) Docherty, R.; Roberts, K.; Dowty, E. Morang — A computer program designed to aid in the determinations of crystal morphology. Computer Physics Communications **1988**, 51, 423–430.

(30) Docherty, R.; Clydesdale, G.; Roberts, K. J.; Bennema, P. Application of Bravais-Friedel-Donnay-Harker, attachment energy and Ising models to predicting and understanding the morphology of molecular crystals. Journal of Physics D: Applied Physics **1991**, 24, 89–99.

(31) Kresse, G.; Hafner, J. Ab initiomolecular dynamics for liquid metals. Physical Review B **1993**, 47, 558–561.

(32) Kresse, G.; Hafner, J. Norm-conserving and ultrasoft pseudopotentials for first-row and transition elements. Journal of Physics: Condensed Matter **1994**, 6, 8245–8257.

(33) Kresse, G.; Furthmüller, J. Efficient iterative schemes for ab initio total-energy calculations using a plane-wave basis set. Physical Review B **1996**, 54, 11169–11186.

(34) Perdew, J. P.; Burke, K.; Ernzerhof, M. Generalized Gradient Approximation Made Simple. Physical Review Letters **1996**, 77, 3865–3868.

(35) Monkhorst, H. J.; Pack, J. D. Special points for Brillouin-zone integrations. Physical Review B **1976**, 13, 5188–5192.

(36) Henkelman, G.; Uberuaga, B. P.; Jónsson, H. A climbing image nudged elastic band method for finding saddle points and minimum energy paths. The Journal of Chemical Physics **2000**, 113, 9901–9904.

(37) Henkelman, G.; Arnaldsson, A.; Jónsson, H. A fast and robust algorithm for Bader decomposition of charge density. Computational Materials Science **2006**, 36, 354–360.

(38) Sanville, E.; Kenny, S. D.; Smith, R.; Henkelman, G. Improved grid-based algorithm for Bader charge allocation. Journal of Computational Chemistry **2007**, 28, 899–908.

(39) Tang, W.; Sanville, E.; Henkelman, G. A grid-based Bader analysis algorithm without lattice bias. Journal of Physics: Condensed Matter **2009**, 21, 084204.

(40) Kolny-Olesiak, J. Recent Advances in the Colloidal Synthesis of Ternary Transition Metal Phosphides. Zeitschrift für Naturforschung A **2019**, 74, 709–719.

(41) Fruchart, R.; Roger, A.; Senateur, J. P. Crystallographic and Magnetic Properties of Solid Solutions of the Phosphides M2P, M = Cr, Mn, Fe, Co, and Ni. Journal of Applied Physics **1969**, 40, 1250–1257.

(42) Ma, J.; Hegde, V. I.; Munira, K.; Xie, Y.; Keshavarz, S.; Mildebrath, D. T.; Wolverton, C.; Ghosh, A. W.; Butler, W. H. Computational investigation of half-Heusler compounds for spintronics applications. Physical Review B **2017**, 95, 024411.

(43) Bartel, C. J.; Trewartha, A.; Wang, Q.; Dunn, A.; Jain, A.; Ceder, G. A critical examination of compound stability predictions from machine-learned formation energies. npj Computational Materials **2020**, 6.

(44) He, Y.; Laursen, S. The surface and catalytic chemistry of the first row transition metal phosphides in deoxygenation. Catalysis Science & Technology **2018**, 8, 5302–5314.

(45) Saal, J. E.; Kirklin, S.; Aykol, M.; Meredig, B.; Wolverton, C. Materials Design and Discovery with High-Throughput Density Functional Theory: The Open Quantum Materials Database (OQMD). JOM **2013**, 65, 1501–1509.

(46) Kirklin, S.; Saal, J. E.; Meredig, B.; Thompson, A.; Doak, J. W.; Aykol, M.; Rühl, S.; Wolverton, C. The Open Quantum Materials Database (OQMD): assessing the accuracy of DFT formation energies. npj Computational Materials **2015**, 1.

(47) Belykh, L. B.; Skripov, N. I.; Belonogova, L. N.; Umanets, V. A.; Schmidt, F. K. Synthesis, properties, and activity of nanosized palladium catalysts modified with elemental phosphorus for hydrogenation. Kinetics and Catalysis **2010**, 51, 42–49.

(48) Belykh, L. B.; Skripov, N. I.; Sterenchuk, T. P.; Gvozdovskaya, K. L.; Sanzhieva, S. B.; Schmidt, F. K. Pd-P nanoparticles as active catalyst for the hydrogenation of acetylenic compounds. Journal of Nanoparticle Research **2019**, 21, 198.

(49) Liu, Y.; McCue, A. J.; Miao, C.; Feng, J.; Li, D.; Anderson, J. A. Palladium phosphide nanoparticles as highly selective catalysts for the selective hydrogenation of acetylene. Journal of Catalysis **2018**, 364, 406–414.

(50) Sampath, A.; Flaherty, D. W. Effects of phosphorus addition on selectivity and stability of Pd model catalysts during cyclohexene dehydrogenation. Catalysis Science & Technology **2020**, 10, 993–1005.